



# Causes and impacts of sea ice variability in the sea of Okhotsk using CESM-LE

Matthew Z. Williams<sup>1</sup> · Melissa Gervais<sup>2,3</sup> · Chris E. Forest<sup>1</sup>

Received: 19 September 2019 / Accepted: 7 December 2020 / Published online: 5 January 2021  
© The Author(s), under exclusive licence to Springer-Verlag GmbH, DE part of Springer Nature 2021

## Abstract

This study provides a holistic view of the coupled ocean-atmosphere-sea ice processes responsible for generating interannual variability in sea ice coverage in the Sea of Okhotsk as well as the atmospheric response to this variability. Simulations from the Community Earth System Model Large Ensemble project are analyzed, providing the ability to elucidate the time evolution of these relationships through weekly lead-lag composite analysis, while maintaining a large number of samples to provide robust conclusions. We find that thermodynamic processes involving anomalous ocean-atmosphere heat fluxes affect the timing of initial sea ice growth in the Sea of Okhotsk as early as November. Low-level wind anomalies in the winter affect the extent to which sea ice fully develops, both through advection of the sea ice itself and through changes in the transport of air masses over the Sea of Okhotsk. In this study, the results synthesize and support a diverse set of mechanisms identified in previous observational studies to be responsible for anomalous sea ice conditions, but in a coupled global climate model framework with a large sample size. We also find evidence that anomalous ocean-atmosphere heat fluxes in the winter can trigger an atmospheric response comprised of a local negative sea-level pressure anomaly and Rossby wave that extends over North America. The sign of the turbulent heat fluxes relative to the sea ice anomalies confirm that this is indeed a lagged response of the atmosphere forced by sea ice anomalies. This validates the Rossby wave train response identified in more idealized model simulations with prescribed sea ice and sea surface temperature by demonstrating that this process also occurs in a more realistic coupled model framework.

**Keywords** Sea-ice growth · Sea of Okhotsk · Sea-ice variability · Atmospheric response to sea-ice anomalies · CESM large ensemble

## 1 Introduction

As a result of anthropogenic climate change, sea ice in the northern hemisphere is experiencing an overall decline—becoming increasingly thinner and covering a smaller spatial extent. Simulations by the Community Earth System Model (CESM) project the central Arctic to become seasonally

ice-free within the next few decades (Jahn et al. 2016). A variety of economic and geopolitical implications will result, such as the opening of trans-Arctic shipping routes (Gascard et al. 2017; Melia et al. 2017). Predicting interannual variability of Arctic sea ice will be important for determining whether shipping routes will be clear of sea ice and safe to pass. There is also considerable interest in how changes in Arctic sea ice might influence atmospheric circulation in the mid-latitudes. If sea ice variability has a significant impact on atmospheric circulation, this could also be a source of predictability for atmospheric variability.

The Sea of Okhotsk (SOK), located south of the Arctic Circle, north of the Kuril Islands and west of the Kamchatka Peninsula (Fig. 1), is already seasonally ice-free and has large interannual variability in its wintertime sea ice coverage (Fig. 2). Thus, sea ice in this region provides a useful test case for understanding the dominant processes involved in producing interannual variability in seasonal ice cover,

✉ Melissa Gervais  
mmg62@psu.edu

<sup>1</sup> Department of Meteorology and Atmospheric Science,  
The Pennsylvania State University, University Park,  
Pennsylvania, USA

<sup>2</sup> Department of Meteorology and Atmospheric Science,  
and The Institute for CyberScience, The Pennsylvania State  
University, University Park, Pennsylvania, USA

<sup>3</sup> Lamont-Doherty Earth Observatory, Columbia University,  
New York, New York, USA



**Fig. 1** The sea of Okhotsk, extending roughly from 45°N to 60°N and from 140°E to 155°E

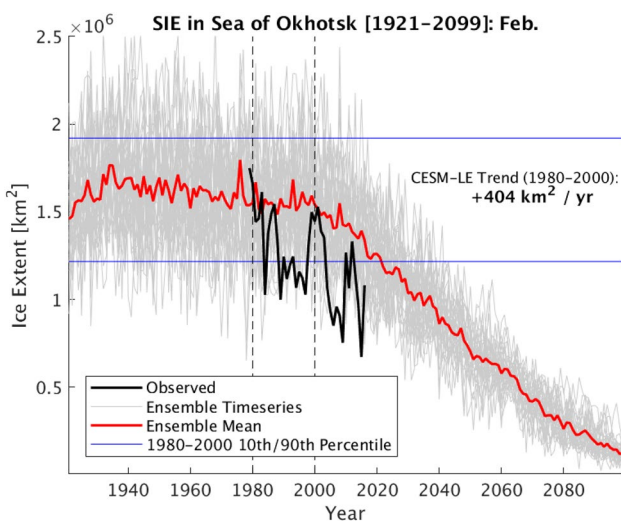


**Fig. 2** CESM-LE representation of February total SIE in the SOK from 1921 to 2099. The dashed vertical lines show the years of this study, 1980–2000. Points in between these dashed lines and above the top blue line (below the bottom blue line) comprise the High (Low) regime cases. Observed SIE from 1979–2016 is shown in the solid black line

although we do expect different Arctic regions to have some different sources of variability. Furthermore, within the SOK, through comparison with observations, it is possible to assess the ability of an Earth system model to represent the causes and impacts of this variability.

Previous studies have shown that the leading mode of sea ice variability in the Northern Hemisphere winter is a “double seesaw” pattern with positive polarity in the SOK and Nordic Seas and negative polarity in the Bering and Labrador Seas (Deser et al. 2000; Ukita et al. 2007; Yamamoto et al. 2006). Many of these studies have found correlations between this mode of sea ice variability and the North Atlantic Oscillation (NAO) or the Arctic Oscillation (AO) that can occur on seasonal (Ogi et al. 2015; Ukita et al. 2007; Ogi and Tachibana 2006; Yamamoto et al. 2006; Deser et al. 2000) to interannual time scales (Ukita et al. 2007). Following Thompson and Wallace (1998), we consider the NAO to be a regional subset of the AO and will refer to both as the NAO/AO. Anomalous surface temperature advections from the NAO/AO can affect sea surface temperature (SST) through changes in ocean-atmosphere heat fluxes. Through such mechanisms shorter time scale atmospheric variability can be integrated by the ocean/sea ice system to produce longer timescales of variability.

Autumn atmospheric forcing has a large impact on winter SOK sea ice (Ukita et al. 2007; Ogi et al. 2015; Ohshima et al. 2006; Sasaki et al. 2007), because the ocean is ice free during Autumn allowing for greater ocean-atmosphere heat flux (Sasaki et al. 2007). In general, October–November surface heat flux from the ocean to the atmosphere in the northwestern SOK is negatively correlated with winter sea ice coverage (Ohshima et al. 2006). SST anomalies in the western Bering Sea, in late autumn and early winter also have a significant negative correlation with maximum SOK sea ice coverage (Nakanowatari et al. 2010). These studies demonstrate how preconditioning of SSTs can increase (inhibit) the formation of sea ice in the winter, either due to anomalously positive (negative) autumn heat fluxes from the sea to the atmosphere or advection of anomalously cold (warm) SSTs.

Although the NAO/AO are useful for explaining the atmospheric impacts on sea ice, many studies have found that they are not able to represent the entirety of the atmospheric forcing signal (Deser et al. 2000; Ukita et al. 2007; Sasaki et al. 2007). Instead, Sasaki et al. (2007) found that the superposition of two Rossby waves in Autumn drives ocean-atmosphere heat fluxes over the SOK. The first wave propagates from the eastern North Atlantic to central Siberia and the second from eastern Siberia to Alaska. When combined, they produce a geopotential height gradient between the Bering Sea and northern Eurasia that drives the heat fluxes. These independent Rossby waves cannot be explained using a single teleconnection index (Sasaki et al. 2007).

More recently, Close et al. (2017) revisited the double seesaw pattern of sea ice variability with a longer observational record and found that the leading mode results from co-variability between the Sea of Okhotsk, the Barents Sea, and the Greenland Sea, with the dominant atmospheric

forcing mechanism being the strength of the Siberian High. Here the strength of the Siberian high is found to be partly responsible for modulating the sea level pressure gradients between the Aleutian Low or the Icelandic Low and the Siberian High, which are important for the SOK and Barents/Greenland Seas respectively. Close et al. (2017) also found that the double seesaw is more apparent during sub-periods of the record, indicating the role of multidecadal variability in these patterns and the limits of examining a relatively short observational record.

In the winter months, mechanical forcing of sea ice by the atmosphere also becomes important for determining the interannual variability in coverage of sea ice in the SOK. The sea-level pressure gradient dictates the low-level wind direction and the type of air mass present over the SOK, both of which likely modulate the ultimate extent of sea ice coverage (Sasaki et al. 2007; Kimura and Wakatsuchi 1999). Kimura and Wakatsuchi (1999) found that mechanical advection from low-level winds that acts to transport sea ice away from the coast is the dominant driver of expansions of the sea ice edge. Thermodynamic ice formation in the winter also occurs but often as a recovery from synoptic time-scale thermodynamic sea ice loss (Kimura and Wakatsuchi 1999).

Sea ice in the SOK can also impact atmospheric circulation as seen in both observational analyses (Alexander et al. 2004; Honda et al. 1999; Mesquita et al. 2011) and modeling experiments with anomalous SOK sea ice (Honda et al. 1999; Mesquita et al. 2011; Screen 2017; Sun et al. 2015). A primary feature of the response is a stationary Rossby wave that extends from the SOK over North America (Alexander et al. 2004; Honda et al. 1999; Screen 2017; Sun et al. 2015). In particular, the greatest potential for anomalous SOK sea ice to impact the atmosphere is in February when the product of total surface heat flux and sea ice extent (SIE) anomalies is maximized (Screen 2017). Associated with this Rossby wave response, sea ice variability in the SOK affects storm track activity in the North Atlantic through cyclone seeding (Mesquita et al. 2011), where transient upper-level troughs formed over the North Pacific in response to SOK sea ice anomalies can eventually lead to enhanced extratropical cyclone formation in the North Atlantic. The response to low sea ice coverage over the SOK and Bering Sea was also found to interfere destructively with the climatological stationary wave, thus enhancing the stratospheric polar vortex (Sun et al. 2015).

In this study, we use the CESM-LE (Kay et al. 2015), a large ensemble of fully-coupled model simulations, to conduct a comprehensive investigation of the coupled processes involved with sea ice coverage in the SOK. Specifically, we consider periods both preceding and following anomalous coverage in February when its potential to impact atmospheric circulation is highest. Previous studies examining

the mechanisms responsible for sea ice variability in the SOK have been predominantly conducted using observations (Deser et al. 2000; Ukita et al. 2007; Yamamoto et al. 2006; Ogi et al. 2015; Ohshima et al. 2006; Sasaki et al. 2007; Kimura and Wakatsuchi 1999; Close et al. 2017). As such, this study will provide an opportunity to investigate the presence of these mechanisms within a global climate model. By using the large ensemble, we can also overcome some issues with a short observational record (Close et al. 2017) and examine the evolution of atmospheric conditions associated with anomalous February SOK ice conditions on a finer time resolution using weekly composites. Furthermore, the atmospheric response to anomalous SOK sea ice has typically been examined in observations (Honda et al. 1999) and global climate model simulations with prescribed sea ice and SSTs (Honda et al. 1999; Alexander et al. 2004; Sun et al. 2015; Screen 2017). This study complements these previous studies by examining these processes in the context of a fully coupled model simulation.

## 2 Data and methods

### 2.1 Model

In this study, we employ the Community Earth System Model Large Ensemble (CESM-LE) simulations (Kay et al. 2015) to identify atmospheric and oceanic conditions associated with anomalous wintertime sea ice coverage in the SOK. The CESM-LE consists of a large ensemble of simulations all branched in 1920 from a single simulation with the only discrepancies between members being small perturbations in the initial air temperature field on the order of  $10^{-14}$  K. Therefore, the non-linear effects of chaotic internal variability in Earth's climate system generate the differences from member to member (Kay et al. 2015), and averaging over multiple members can help eliminate the effects of this variability and enhance the signal-to-noise ratio. For this study, we employ the original 30 ensemble members.

These simulations are run with the fully coupled CESM1 model consisting of atmosphere, ocean, land, and sea ice components. The atmospheric component, Community Atmosphere Model version 5 (CAM5) (Hurrell et al. 2013), has 30 vertical levels and a horizontal resolution of  $1.25^\circ \text{lon} \times 0.9^\circ \text{lat}$ . The land component model is the Community Land Model version 4 (CLM4) (Lawrence et al. 2011; Oleson et al. 2010) with the same horizontal resolution as CAM5. The ocean and sea ice models, Parallel Ocean Program version 2 (POP2) (Smith et al. 2010) and Community Ice Code version 4 (CICE4) (Hunke and Lipscomb 2008) respectively, are on a tripole grid with approximately  $1^\circ \times 0^\circ$  horizontal resolution and the POP2 model has 60 vertical levels. CICE4 represents sea ice with five thickness

categories (Rothrock 1975; Thorndike et al. 1975), uses an energy-conserving thermodynamic scheme (Bitz and Lipscomb 1999), and includes boundary conditions forced by both atmospheric and oceanic stresses (Hunke and Dukowicz 2002). As compared to observations, the CESM-LE has the best representation of spatial patterns of interannual sea ice variability among the Coupled Model Intercomparison Project Phase 5 (CMIP5) models (England et al. 2019). Similar to other CMIP5 models however, the CESM-LE has a positive northern hemisphere annual-mean sea ice bias (England et al. 2019; Rosenblum and Eisenman 2017), that is indicative of the forced response being too small in the model (Rosenblum and Eisenman 2017).

There are advantages and disadvantages of using the CESM-LE for this study. Similar to the real climate system, these fully coupled model simulations include atmosphere-ocean-sea ice interactions that are important for understanding sea ice variability. However, much like observations, this model framework limits our ability to disentangle cause and effect within these coupled processes. For example, assessing the impact of anomalous SOK sea ice on atmospheric circulation is difficult due to the simultaneous role of atmospheric circulation in the generation of SOK sea ice anomalies. Comparison of results found here to more idealized prescribed SST and sea ice modeling studies can help to overcome this issue. One of the greatest advantages of using the CESM-LE is the large sample size, which leads to higher statistical significance. Most previous studies employ seasonal or monthly averages in order to smooth out synoptic-scale variability. With the large sample size that the CESM-LE provides, that variability is effectively reduced even when considering weekly averages. This shortens the required time increments for analyzing the progression of conditions both preceding and following winters of anomalous sea ice.

## 2.2 Observations

For comparison with the modeled connection of atmospheric and oceanic conditions with SOK sea ice variability, we used multiple observation-based products for the atmosphere, ocean, and sea ice. The ERA-interim reanalysis product (Dee et al. 2011) provides atmospheric information with horizontal resolution of approximately  $80\text{ km} \times 80\text{ km}$  on 60 vertical levels. COBE SST data (Ishii et al. 2005) contains monthly-averaged SST data on a  $1^\circ$  latitude  $\times 1^\circ$  longitude grid. The sea ice product, NOAA/NSIDC Climate Data Record of Passive Microwave Sea Ice (Meier et al. 2017; Peng et al. 2013), implements a combination of two algorithms to yield more accurate SIC estimates from satellite data retrieval. These SIC estimates have a horizontal resolution of  $25\text{ km} \times 25\text{ km}$ .

## 2.3 Methods

We analyzed SOK sea ice coverage and atmospheric variables for the years of 1980–2000, when both the observational data products were available and the CESM-LE ensemble-averaged sea ice extent (SIE) showed no significant trend. In this study, we conduct a composite analysis over anomalously high and low sea ice years, which requires that the mean be constant over the period of study. For example, assuring a constant mean will avoid biasing identified high sea ice years towards the start of the period of study and vice versa for the low sea ice years. We defined SIE as the total area of grid boxes having at least 15% sea ice concentration (SIC), where SIC is the fraction of a grid box covered by sea ice. The CESM-LE has both a large sample size and a wide range of variability in SIE over the analysis period, which is ideal for identifying a coherent signal in conditions associated with extreme SIE. Within the model analysis, we defined the thresholds for extreme cases as the 10th and 90th percentiles of SIE values in February for all ensemble-year combinations (e.g., ensemble member 3 in 1986) providing a total sample size of 630 (30 ensembles  $\times$  21 years). We classified individual ensemble-year combinations with SIE values less (greater) than the tenth (ninetieth) percentile as belonging to the Low (High) sea ice regime for a total of 63 samples in each regime (Fig. 2).

For the observations, we chose the 5 years of least (greatest) February-averaged SIE to comprise the Low (High) regime. Those years, ordered from most-extreme to least-extreme, were 1989, 1984, 1997, 1994, and 1991 (1980, 1983, 1987, 1999, and 1986). These instances of observed extreme February SIE in the SOK lie outside of roughly the 25th and 75th percentiles of the observational record. As a result, when the model is compared to the observations, we utilize the 25th and 75th percentiles of SIE values in February, which will be referred to as the Low 25th and high 75th sea ice regimes.

Previous studies involving atmosphere and SOK sea ice relations have analyzed monthly-averaged (Screen 2017; Yamamoto et al. 2006) or seasonally-averaged (Alexander et al. 2004; Close et al. 2017; Honda et al. 1999; Sasaki et al. 2007) fields. However, atmospheric forcing of and response to anomalous sea ice coverage can occur on timescales of a few days (Fang and Wallace 1994). To gain more insight into these processes that have shorter timescales, in the present study, we analyzed a progression of weekly-averaged, lagged composite anomaly fields in the CESM-LE. The anomalies are computed for the Low or High sea ice regime with respect to the average over all ensemble members and years. To investigate the atmospheric and oceanic conditions associated with anomalous SIE for the Low and High sea ice regimes, we evaluated lagged composite anomalies for turbulent heat flux (THF), mean sea-level pressure (SLP),

850 hPa potential temperature ( $\theta_{850}$ ), 500 hPa geopotential height ( $Z_{500}$ ), 500 hPa wave activity flux ( $W$ ), 850 hPa wind ( $U_{850}$ ), near-surface wind ( $U_{BOT}$ ), and sea surface temperature (SST). THF is the sum of sensible and latent heat flux. Wave activity flux is computed following (Takaya and Nakamura 2001) on the 500 hPa surface. Daily values for the necessary variables are provided on a limited number of pressure levels in the CESM-LE and so only the horizontal components of the wave activity flux can be computed on a single pressure level. We first included the monthly-averaged fields for August through November, so as to analyze potentially important features such as persistent SST anomalies or atmospheric waves. The weekly-averaged portion was then computed spanning the 20 weeks from the week beginning on November 23 to the week ending on April 11. Statistical significance of the lagged composite anomalies are computed using the two-sided Student's t-test at the five percent level.

Due to the small sample size in the observations, we did not conduct weekly composites. Instead, an additional set of monthly-averaged lagged composites were produced for both the observations and the CESM-LE Low 25th regime to facilitate comparison between the two. Statistical significance was computed using a two-sided Student's t-test. However, as a consequence of the small sample size in the observations, these composite anomalies were rarely deemed significant.

For brevity, only the results from the Low regime are shown in the next section. We expect that the same mechanisms are responsible for both anomalously high and low wintertime SOK sea ice coverage. Results from the High regime are generally similar but of opposite sign to those from the Low regime (not shown).

### 3 Results

#### 3.1 Seasonal cycle

We show the seasonal cycles for both the model and the observations (Fig. 3) including the mean, 10th to 90th percentiles, and composites of the High and Low SIE regimes. By comparing the modeled and observed SIE seasonal cycle, we find a notable bias in the model SIE in both the timing of the seasonal sea ice cycle and the maximum SIE value. In the model, the SOK is typically ice-free from July to November and the average SOK SIE reaches a maximum in March of approximately  $1.75 \times 10^6 \text{ km}^2$ . In the observations, SOK sea ice begins to grow in September and the mean reaches a maximum in February at a smaller value of approximately  $1.25 \times 10^6 \text{ km}^2$ .

In addition to the biases between the observed and modeled means, we also find differences in the shape of

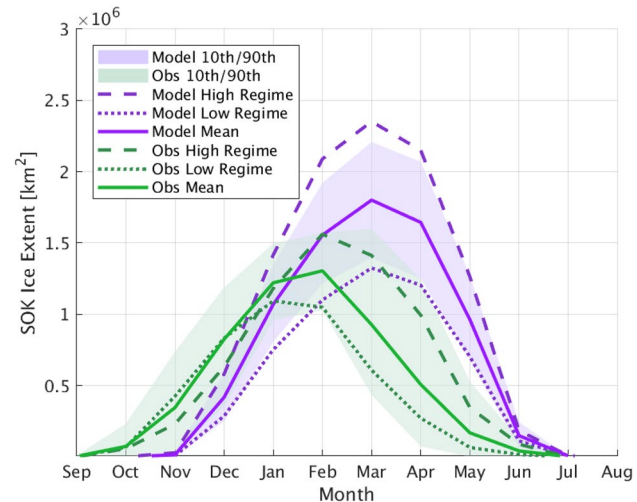


**Fig. 3** Annual cycle of SIE in the SOK. CESM-LE (observed) SIE curves are purple (green). The shaded regions are bounded by the 10th and 90th percentiles for each month. The solid curves depict the monthly means for the modeled and observed SIE. The dashed (dotted) curves depict the composite-mean SIE for the High (Low) regime

the seasonal cycles of the High and Low regimes. In the model, High and Low regime curves remain near the 90th and 10th percentile values for each month from December to May. Unlike the model, the observed Low regime SIE closely follows the mean SIE until January, after which we see lower values of SIE throughout the rest of the ice covered season. The High regime has lower SIE than average through the months of October to December, after which there is a marked increase in SIE until February (Fig. 3). The observations consist of only 5 members, each of whom have large differences in their seasonal cycles that impact the ensemble mean (not shown). It is difficult to assess whether the seasonal cycle differences between the observations and the model in both regimes are the result of these sampling limitations or of differences in mechanisms.

#### 3.2 Multi-seasonal SST anomaly presence

The earliest signs of conditions preceding anomalous sea ice coverage occur in the SST field and are identified in the CESM-LE progression of monthly-averaged SST composite anomalies in the North Pacific (Fig. 4). Positive SST anomalies tend to exist in the winter 1 year prior to anomalously low sea ice along the Kamchatka Peninsula coast and into the western Bering Sea (Fig. 4). SST anomalies also appear over the eastern SOK and Sea of Japan in the spring prior in the observations (not shown). These results are consistent with Deser et al. (2003), which showed that SSTs in this region have a fairly high interannual autocorrelation. The magnitudes of the SST composite anomalies are highest in

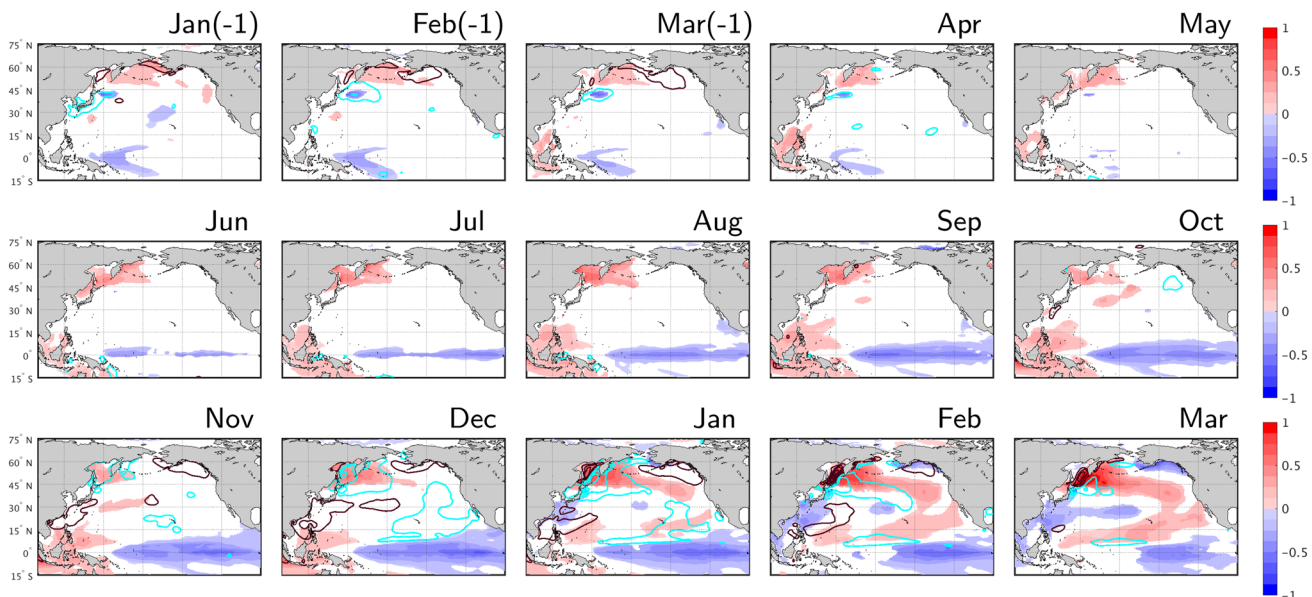


**Fig. 4** Modeled monthly SST anomalies (shaded) and THF anomalies (contours) for the Low regime. Top row contains monthly-averaged values, while other rows contain weekly-averaged values. Contours begin at  $\pm 10 \text{ W m}^{-2}$  and have an interval of  $20 \text{ W m}^{-2}$ . Positive (negative)

THF anomalies are shown by maroon (cyan) contours and correspond to heat transfer out of (into) the surface. Only SST anomalies that are statistically significant at the  $\alpha=0.05$  level are shown

February and March at the peak of the sea ice anomalies and have a secondary peak in the late summer months in the model composites (Fig. 4).

In addition to these local SST anomalies, negative SST anomalies develop in the equatorial Pacific over the preceding summer. The pattern of these SSTs is La Niña-like but of an order of magnitude smaller with anomalies reaching 0.4 K. Over the summer and early fall (August–October) there is no evidence of any ENSO teleconnection in the 500 hPa geopotential heights. The potential role for teleconnection associated with tropical Pacific SSTs to impact the Aleutian Low cannot be discounted from November to March. Progressing into the winter, additional significant anomalies develop across the North Pacific that are of the same magnitude as those in the tropical Pacific anomalies. The SST anomaly pattern from January through March over the North Atlantic is less reminiscent of a La Niña, but is closer to a recently identified pattern of decadal SST variability (Gu and Gervais 2020).

### 3.3 Autumn thermodynamic preconditioning

Multiple studies have demonstrated the importance of thermodynamic conditions in setting the stage for anomalous wintertime sea ice coverage in the SOK. Consistent with Ohshima et al. (2006), negative turbulent heat flux (THF) anomalies appear over the northwestern SOK in November and grow in magnitude and spread over the remaining

portions of the sea into December (Fig. 4). These negative THF anomalies indicate a reduction of late autumn oceanic heat loss to the atmosphere compared to average conditions. The opposite effect occurs prior to anomalously high sea ice coverage with increases in late autumn oceanic heat loss (not shown).

THF is modulated by multiple factors including temperature contrast between the sea surface and low-level atmosphere, as well as low-level atmospheric relative humidity and wind speed. In November, the aforementioned temperature contrast is altered, with SST and  $\theta_{850}$  anomalies both present for the SOK (Figs. 4 and 6). Wind speed is also reduced at this time, as easterly wind anomalies oppose the westerly mean wind (Fig. 5; mean wind not shown). This implies that both anomalous air-sea temperature contrast and decreased wind speed in autumn may contribute to the THF anomalies in the SOK.

Low-level winds in the region surrounding the SOK are modulated through the relative strengths and locations of both the Aleutian low and Siberian high. In the  $Z_{500}$  composite anomalies, the pattern resembles that of a stationary Rossby wave that originates from the eastern North Atlantic and extends into north-central Asia in October/November where it impacts the Aleutian Low and Siberian High (Fig. 7). This  $Z_{500}$  pattern is similar to the Rossby wave shown by Sasaki et al. (2007) in the observational record that extends from the eastern North Atlantic to central Siberia and impacts Autumn SOK THF, although there are some differences in the locations of the centers of action.

However, the wave activity flux does not support that these  $Z_{500}$  anomalies are due to a stationary Rossby wave (Fig. 7). Regardless, this particular circulation structure favors anomalous low-level flow over the SOK from the central North Pacific, which establishes a milder, maritime air mass that tends to persist for multiple weeks and helps explain the  $\theta_{850}$  anomalies in the autumn prior to abnormal SOK February sea ice coverage (Fig. 6). Therefore, during October and November, this pattern may produce conditions that are conducive to altering the exchange of heat between the sea surface and the atmosphere, thereby changing the timing of initial sea ice formation in the SOK.

### 3.4 Winter forcing

Once sea ice has developed, dynamic factors such as the direction of low-level winds also become important for determining to what extent sea ice will grow in the SOK. For the Low regime, low-level wind anomalies throughout the winter are primarily from the east-southeast over the southeastern half of the SOK (Fig. 5). These wind anomalies are present in conjunction with a noticeably weaker Aleutian low, as demonstrated by the anticyclonic SLP anomalies over the North Pacific (Fig. 7). These anomalous low-level winds allow for a more prevalent maritime air mass over the SOK (Fig. 6), which may prevent sea surface cooling over the southeastern SOK necessary for new sea ice growth in the winter months.

In addition to the thermodynamic effects, the anomalous low-level winds can mechanically inhibit the expansion of preexisting sea ice into the southeastern SOK. This effect is seen throughout December into mid-February opposing the direction of sea ice expansion (Fig. 5) because the wind anomalies are oriented in a nearly perpendicular manner to the sea ice edge. A similar but opposite mechanism occurs during the High regime, with wind anomalies aiding the sea ice expansion to promote additional sea ice growth in this season (not shown).

### 3.5 Atmospheric response to anomalous wintertime SOK sea ice forcing

Previous studies have shown that THF anomalies produced due to anomalous sea ice coverage in the SOK can provide forcing for an atmospheric response (e.g., Screen 2017; Honda et al. 1999; Alexander et al. 2004; Sun et al. 2015). This can be seen from December to February when THF anomalies over the central SOK transition from negative to positive, coincident with the advancement of the sea ice edge (Fig. 5). In the winter, there are typically positive turbulent heat fluxes from the ocean to the atmosphere. These are larger near the sea ice edge as cold air masses are advected from ice covered regions over the open ocean. Anomalously

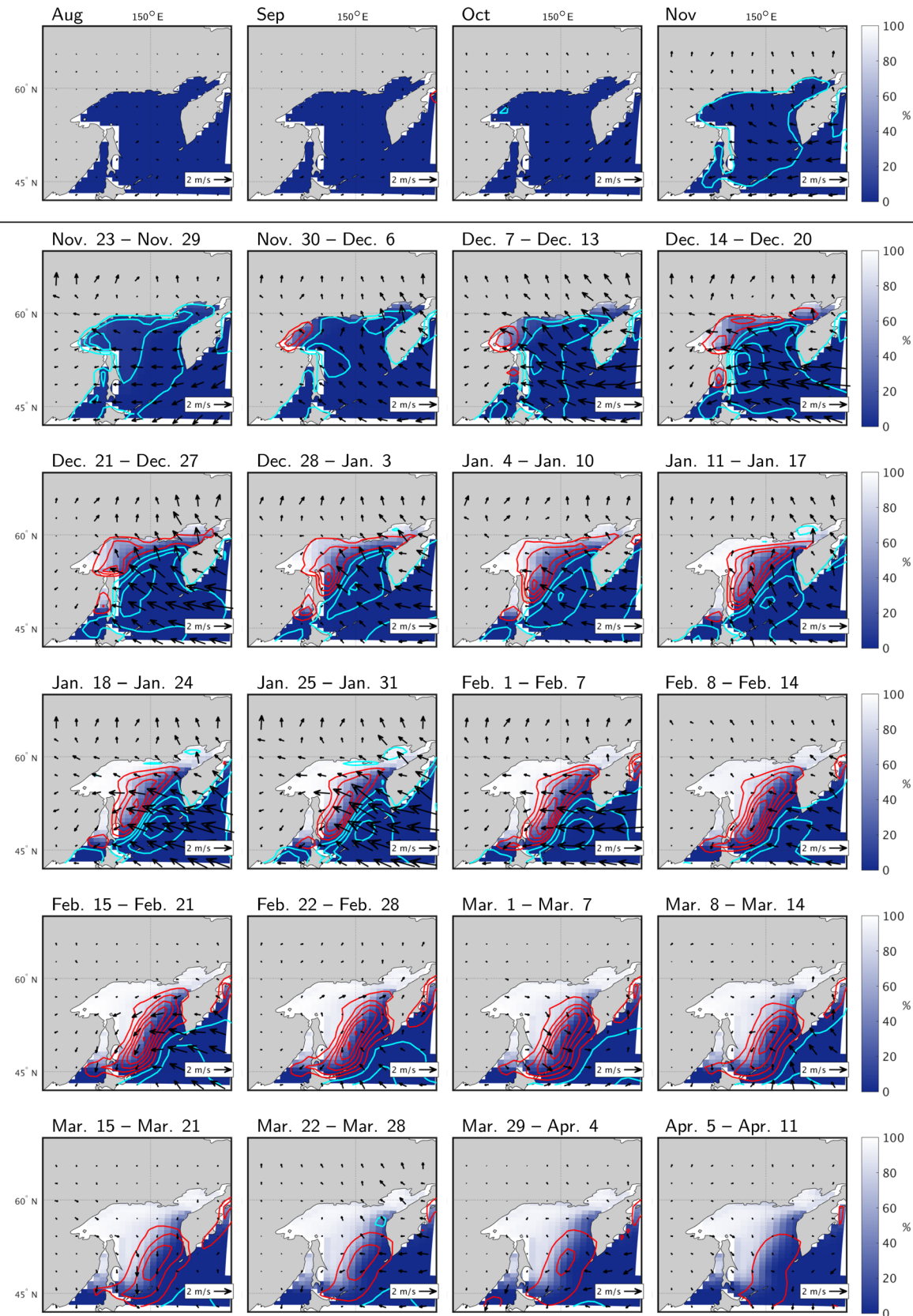
low sea ice effectively shifts the sea ice edge and the associated THF maximum closer to shore. Consequently, as sea ice begins to advance [November 30–December 6], a dipole in THF anomalies develops with positive anomalies associated with anomalously low SIE and negative anomalies in the former region of maximum THF (Fig. 5). Throughout the month of February [from February 1–February 7 to February 22–February 28] the positive anomalies become stronger than the negative anomalies, exceeding  $100 \text{ Wm}^{-2}$  peaking in the last week of February [February 22–February 28].

The transfer of heat from the sea surface into the atmosphere, would force a positive low-level temperature anomaly. A localized positive  $\theta_{850}$  anomaly exists to the southeast of the SOK during the weeks of February 15–February 21 through March 8–March 14 (Fig. 6) and is consistent with the atmospheric response to such THF anomalies. However, this cannot be separated from the forcing mechanism for low sea ice discussed above. The positive SLP anomaly over the SOK is reduced and a negative SLP anomaly develops to the south of the SOK (Fig. 7 [February 15–February 21 and March 8–March 14]). Concurrently, we see a shift of anomalous near-surface wind direction from east-southeasterly to northwesterly over the south-central SOK (Fig. 5 [from February 1–February 7 to March 1–March 7]).

During the week of March 8–March 14, the pattern of  $Z_{500}$  anomalies resembles the Rossby wave response similar to that shown in Honda et al. (1999) and Screen (2017). There is also a divergence of the wave activity flux over the SOK region where there are anomalous heat fluxes (Fig. 7). The wave activity flux continues to follow the  $Z_{500}$  and SLP wave train toward North America. This provides evidence of a stationary Rossby wave response to SOK sea ice. These results are in keeping with the interpretation of Takaya and Nakamura (2001) who used the modeling results of (Honda et al. 1999) with high and low SOK sea ice forcing as an example of the use of wave activity flux to identify stationary Rossby waves.

There is evidence of Rossby wave activity emanating from the SOK region as far back as the November 30–December 6 composite (Fig. 7) when the first heat flux anomalies begin to form (Fig. 5). However, a clear Rossby wave train in the  $Z_{500}$  field does not emerge until March 8–March 14, but rather the weakened Aleutian low thought to be responsible for the low ice conditions remains the most dominant feature in the  $Z_{500}$  field through the majority of the winter. This may be indicative of the challenge in separating forcing from response in a fully coupled context.

In summary, our results demonstrate that there is a stationary Rossby wave response to anomalous SOK sea ice within the fully coupled CESM-LE. With low SOK sea ice there is a dipole in anomalous surface heat fluxes that can force a stationary Rossby wave response. This is most clearly seen in March 8–March 14 composites of wave activity flux,



**◀Fig. 5** Modeled total sea ice concentration (shaded) with THF anomalies (contours) and near-surface wind anomalies (arrows) for the Low regime. Top row contains monthly-averaged values, while other rows contain weekly-averaged values. Contours begin at  $\pm 10 \text{ Wm}^{-2}$  and have an interval of  $20 \text{ Wm}^{-2}$ . Positive (negative) THF anomalies are shown by red (cyan) contours

$Z_{500}$ , and SLP anomalies. This wave train is similar to that in Honda et al. (1999) and Screen (2017), specifically in the latter which uses the same model as the current study. In these studies, atmospheric models are forced with prescribed sea ice and SSTs and so direct attribution can be made to differences in SOK sea ice condition.

### 3.6 Comparison to observations

In the previous section, we identified conditions associated with February sea ice in the SOK within the CESM-LE model simulations. To directly compare our model results to observations, we compute a series of monthly lagged composite anomalies for the five lowest February SIE years in observational products and the Low 25th regime in the CESM-LE. In this analysis, there are several caveats that must be considered. There are biases in the model seasonal cycle both in terms of timing and maximum extent that might impact the coupled interactions between the atmosphere-ocean-sea ice systems. Consequently, overestimates of SIE anomalies still occur even when comparing to the 25th percentile of model SIE due to model biases. Furthermore, the small number of observations leads to a very small signal to noise ratio, limiting the ability to detect and generalize the processes involved in producing anomalous SIE in the SOK within the observational record. Nevertheless, it is vital that such comparisons to observations be conducted, as such these comparisons will be shown with an understanding of the limitations.

Comparisons between the model and observations for SIC, THF, and near-surface wind anomalies demonstrate the impact of biases in the representation of sea ice in the model as well as some broad agreement on mechanisms associated with anomalous sea ice. The model bias towards a delayed seasonal cycle and higher maximum sea ice extent are evident within the Low 25th regime composites (Fig. 8), resulting in higher sea ice concentrations in February sea ice in the model than the observations. There is however broad agreement in the role of THF in the generation and response to anomalous sea ice. There is a broad decrease in THF from the ocean to the atmosphere in December (Fig. 8). A dipole in THF associated with the change in sea ice edge then occurs in both the model and the observations, although it is displaced further east in the model following the mean bias in the sea ice edge (Fig. 8). The magnitude of the THF anomalies are also somewhat larger in the model. Although

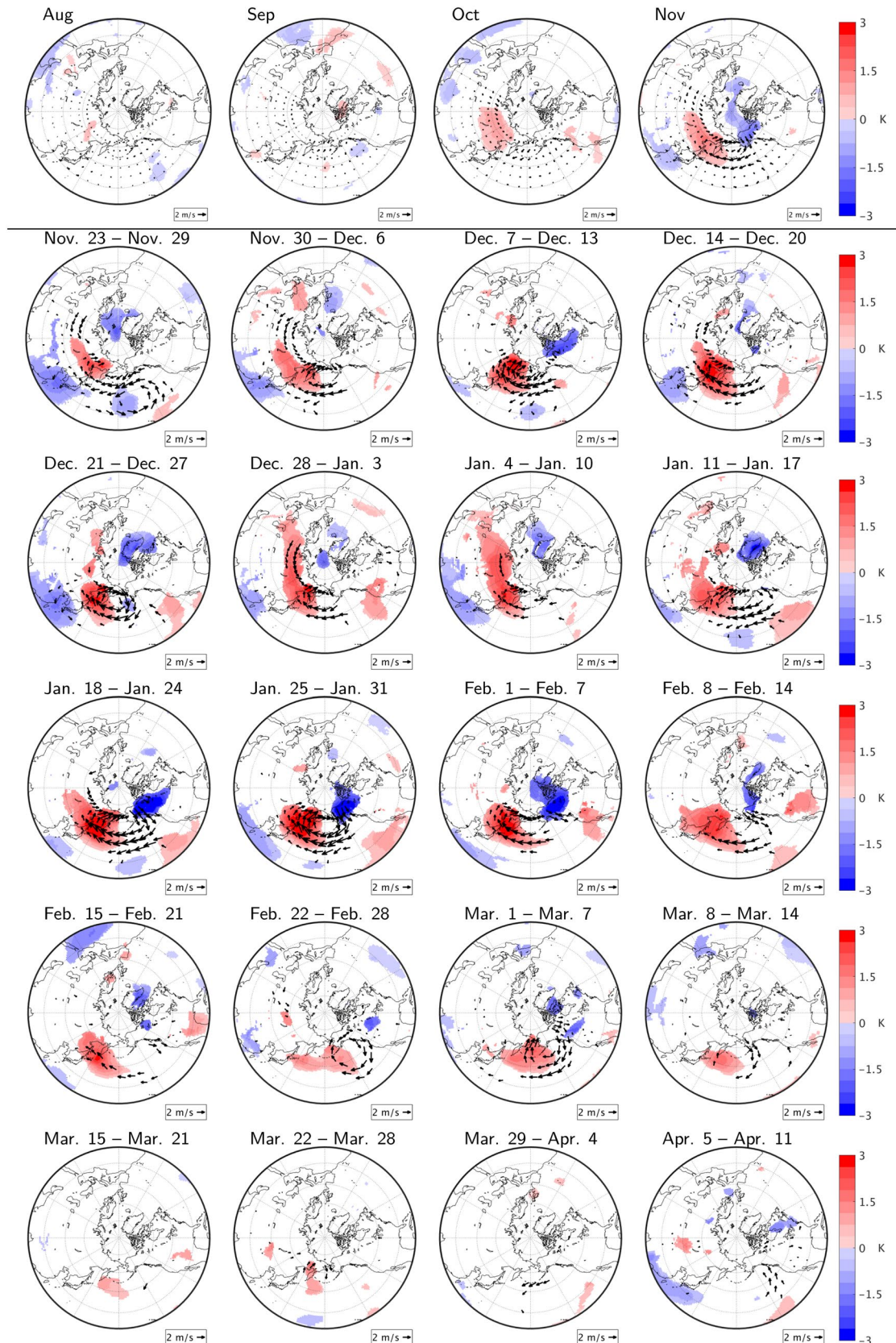
the details in the location of the sea ice concentration changes and associated THF differ according to the model biases, the main mechanisms identified above do occur in both the model and the observations.

Near-surface winds can be important for both advection of warmer air masses and mechanical forcing of sea ice. In the model, anomalous easterly/southeasterly near-surface winds are associated with the Low 25th regime from November to December (Figs. 5, 8). In the observations there are smaller anomalous easterly near-surface winds in January only, with little southerly component (Fig. 8). This is consistent with the large scale forcing where there are larger and more eastward shifted positive  $Z_{500}$  and SLP anomalies in the model associated with a weakened Aleutian Low in December (Fig. 9). In the observations, the positive anomaly in the North Pacific expands over the SOK in January but is still weaker than in the model and is statistically insignificant (Fig. 9). It is unclear if this is a result of the small sample size in the observations or is symptomatic of a larger role for mechanical forcing of sea ice by the atmosphere in the model as compared to the observations.

In February, the observations show a negative SLP anomaly to the east of the SOK, which is consistent with the atmospheric response to sea ice but is not found in the model. It is unclear whether this is due to the persistence of the stronger positive SLP anomaly seen in the model in January, a weaker sea ice response in the model as compared to the observations, or the result of the small sample size in the observations. During March, there is a Rossby wave like pattern in geopotential heights in the model that traverses North America (Fig. 9), however the Low 25th regime has a smaller area of statistical significance than the Low regime both in weekly (Fig. 7) and monthly averages (not shown). Although the observations lack statistical significance, a similar pattern can be seen in the observations (Fig. 9) and the strength of these anomalies is somewhat larger than in the model. This provides some evidence that the Rossby wave response is well captured in the model, although it is possible that the amplitude of the response is somewhat muted.

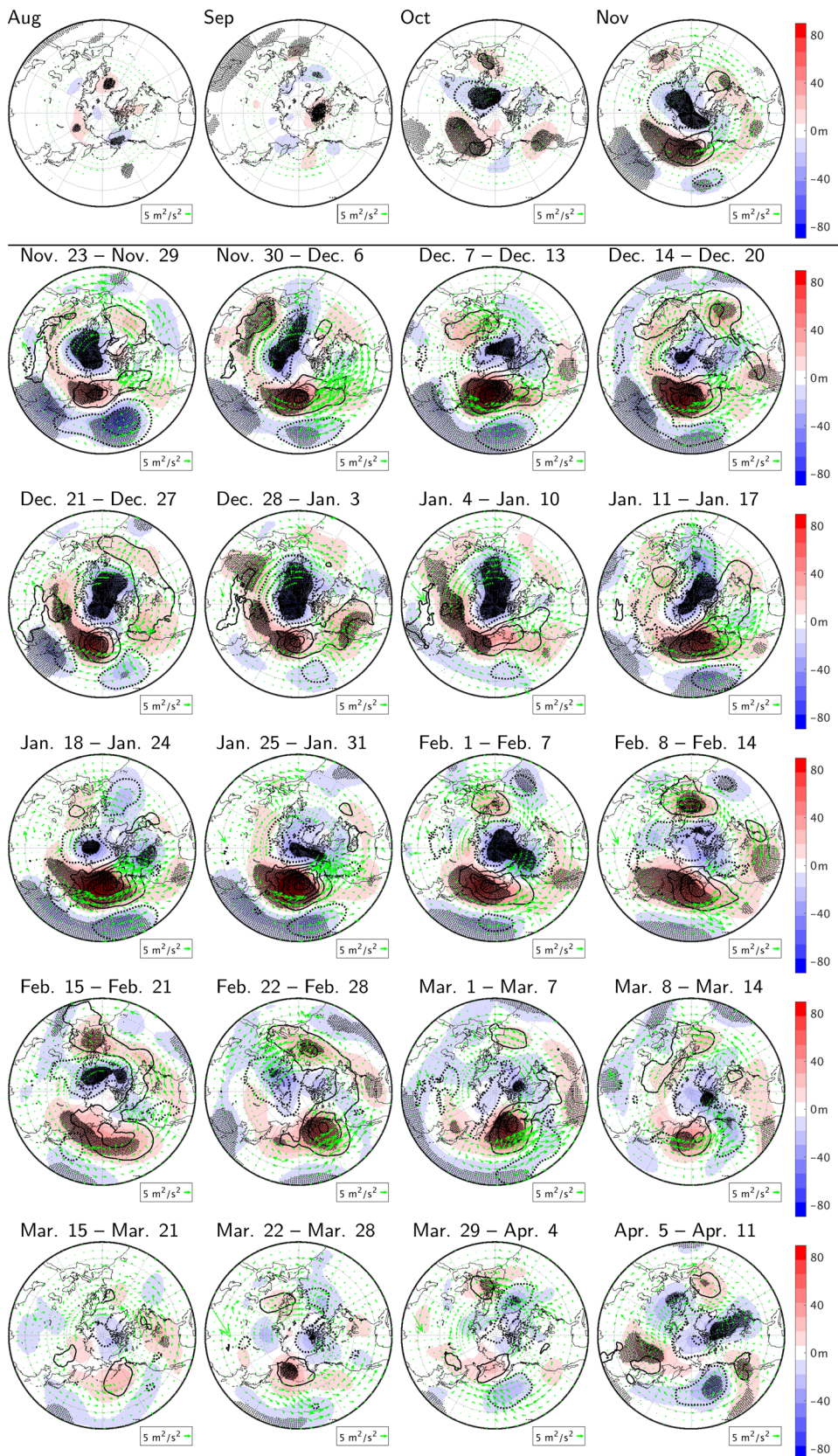
## 4 Conclusions

This study provides a comprehensive view of the lead-lag relationships through which the atmosphere-ocean-sea ice system both produces and responds to sea ice variability in the SOK. Employing both the CESM-LE simulations and observations, we investigated the mechanisms responsible for producing anomalous February sea ice coverage in the SOK and the atmospheric response to these anomalies. The use of a large ensemble of model simulations provides a robust sample size that is not possible through the use of



**Fig. 6** Modeled 850 mb atmospheric anomalies:  $\theta_{850}$  anomalies (shaded) and wind anomalies (arrows) for the Low regime. Top row contains monthly-averaged values, while other rows contain weekly-averaged values. Plotted anomalies are statistically significant at the  $\alpha=0.05$  level

**Fig. 7** Modeled 500 mb geopotential height anomalies (shaded), sea- level pressure anomalies (contours), and horizontal wave activity flux at 500 hPa for the Low regime. Top row contains monthly- averaged values, while other rows contain weekly-averaged values. Contours begin at  $\pm 1$  mb and have an interval of 2 mb. Positive (negative) SLP anomalies are shown by solid (dotted) contours. Geopotential height anomalies are stippled if statistically significant at the  $\alpha = 0.05$  level



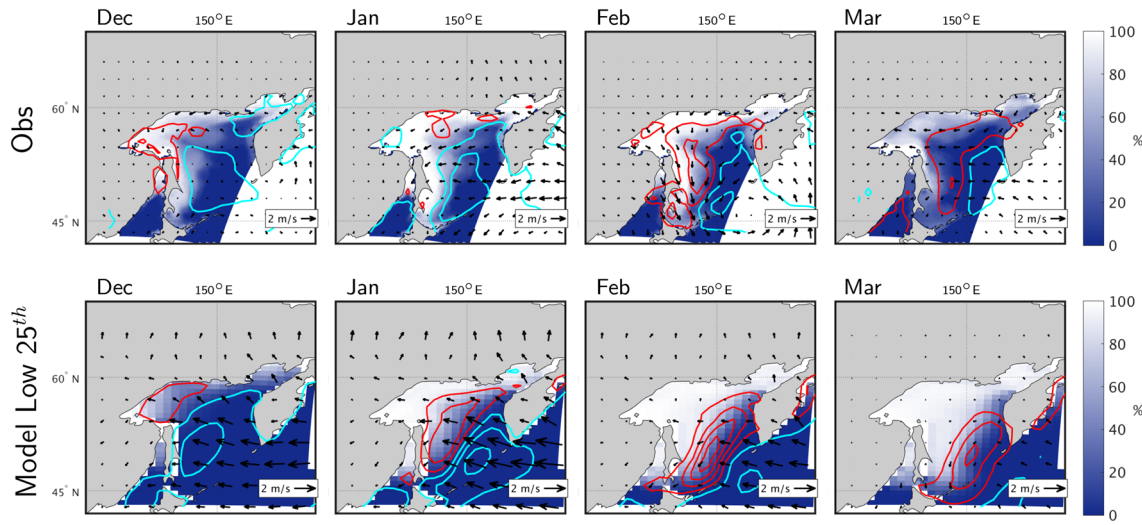


**Fig. 8** Observations (top) and model Low 25<sup>th</sup> (bottom) monthly composite sea ice concentration (shaded) with turbulent heat flux anomalies (contours) and near-surface wind anomalies (arrows) for

the Low regime. Contours begin at  $\pm 10 \text{ Wm}^{-2}$  and have an interval of  $20 \text{ Wm}^{-2}$ . Positive (negative) THF anomalies are shown by red (cyan) contours

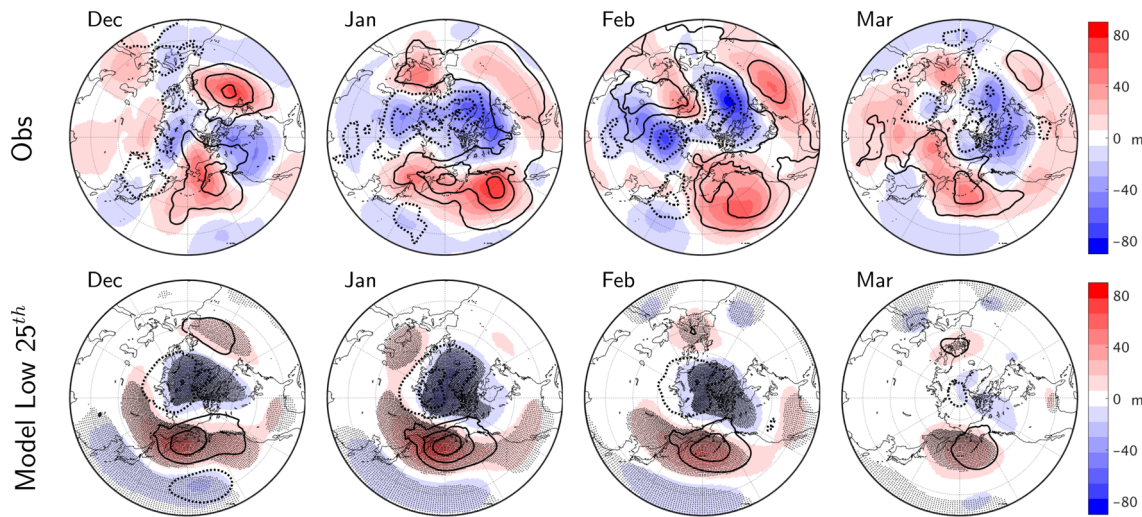


**Fig. 9** Observations (top) and model Low 25<sup>th</sup> regime (bottom) monthly composite 500 mb geopotential height anomalies (shaded) and sea level pressure anomalies (contours) for the Low regime. Top row contains monthly-averaged values, while other rows contain

weekly-averaged values. Contours begin at  $\pm 1 \text{ mb}$  and have an interval of  $2 \text{ mb}$ . Positive (negative) SLP anomalies are shown by solid (dotted) contours. Geopotential height anomalies are stippled if statistically significant at the  $\alpha=0.05$  level

observations alone. Furthermore, it enables us to examine the weekly progression of conditions associated with anomalous SIE, providing a unique view of the entire temporal evolution of the problem. Our results support previous observational and modeling studies that have examined the individual pieces of these complex atmosphere-ocean-sea ice relationships. They also demonstrate the ability of the CESM to represent the dominant mechanisms responsible for SOK sea ice variability and the impacts of anomalous SOK sea ice on the atmosphere.

We find that February SOK sea ice variability in the CESM-LE is influenced by a multitude of factors at various time lags. Extending back to the prior winter, SST anomalies exist in the SOK and western Bering Sea. These reach a temporary peak in magnitude during the summer prior to the SOK sea ice anomalies. In Autumn, low-level atmospheric temperature anomalies then lead to changes in THF that precondition SSTs in the SOK. This thermodynamic mechanism can impact early winter sea ice growth. Once sea ice growth has begun in the winter, the advancement of

the sea ice edge is influenced by advection of sea ice by low-level winds forced by an anomalous SLP gradient between the Siberian high and the Aleutian low.

From January to March, there are significant SST anomalies throughout the North Pacific. The pattern of these anomalies is similar to a newly identified pattern of decadal time scale variability (Gu and Gervais 2020). The relationship between this pattern of variability and atmospheric circulation remains an open question. In the CESM Decadal Prediction Large Ensemble (DPLE) simulation, where the fully coupled CESM model is initialized from an ocean-sea ice simulation forced with observed atmospheric conditions, one of the few regions where initialized decadal predictions are more skillful than uninitialized simulations was in the SOK (Yeager et al. 2018). Further exploration of atmosphere-ocean interactions involved in this new pattern of decadal variability in the Pacific and the potential relationship to SOK sea ice would be an interesting avenue for further research.

Through direct comparison with observations, we demonstrate the ability of CESM-LE to represent mechanisms that force anomalous SOK sea ice. Some differences do exist between the observations and the model representation of these processes. For example the model has larger near-surface wind anomalies corresponding to anomalous SLP in the Aleutian Low that begin one month prior to those in the observations. However, given the limited number of observation it is difficult to determine whether this is the result of the small sample size in the observations or deficiencies in the CESM-LE representation of the mechanisms themselves. In general, the CESM-LE has shown considerable ability to represent these various processes identified in previous literature and in the observations shown here.

In February, THF anomalies in proximity to the average sea ice edge indicate abnormal heat transfer between the surface and the atmosphere. These THF anomalies are associated with a dynamic response in the atmosphere above with a local SLP anomaly and the excitation of a Rossby wave that extends across the North Pacific basin and terminates over North America. This type of response is also shown in the observations, although with the small sample size few of the observed anomalies are statistically significant. One notable difference between the model and the observations is a more clear development of local pressure anomalies associated with SOK SIE in the observations. Our results are consistent with previous work examining the impact of sea ice anomalies on atmospheric circulation using prescribed SSTs and sea ice (Alexander et al. 2004; Honda et al. 1999; Screen 2017). The similarity of these results to idealized modelling studies combined with the wave activity flux analysis, time lag of the relationships and the sign of the turbulent heat fluxes relative to the sea ice anomaly together suggest that this is indeed an atmospheric response to sea

ice anomalies. The identification of this response within the more realistic CESM-LE simulation serves to validate the Rossby wave train response identified in the presence of atmosphere-ocean-sea ice coupling.

The impact of sea ice variability in the SOK on atmospheric circulation has implications for the potential modification of atmospheric mean circulation and variability as sea ice declines with anthropogenic warming. For example, Gervais et al. (2016) applied self-organizing maps to daily equivalent potential temperatures in the CESM-LE experiments under RCP8.5 warming and found that patterns with larger anomalies over north American associated with enhanced ridging and toughing become more frequent in the future. They hypothesized that localized sea level pressure anomalies and subsequently downstream responses associated with sea ice loss in the western Arctic may be responsible.

(Blackport et al. 2019) examined the potential for the Bering-Chukchi Seas to impact temperature extremes over North America. They utilized the sign of THF anomalies relative to sea ice anomalies to determine whether the atmosphere was impacting the sea ice, where low sea ice accompanied by positive THF anomalies from the ocean to the atmosphere implied that the ocean was forcing the atmosphere and vice versa. Blackport et al. (2019) conclude that the relationship between Bering-Chukchi sea ice and North American temperature extremes is due to the simultaneous impact of internal atmospheric variability on sea ice and North American temperatures, and not a response to low sea ice. In contrast, our lagged THF composites based on Low February SOK sea ice show that the atmosphere is influencing the sea ice in November, in early winter we have a dipole in THF associated with the modified sea ice edge, and by March positive THF dominates the region. This implies that sea ice is predominantly influencing the atmosphere in March. This is consistent with (Screen 2017) who, in an idealized modelling study, showed that there is a robust Rossby wave response to SOK sea ice anomalies but not to Bering-Chukchi sea ice anomalies. The impact of sea ice loss on atmospheric circulation is highly dependent on the location of the sea ice and in this case could be the result of the closer proximity of the SOK to the North Pacific jet.

The impact of interannual SOK sea ice variability on atmospheric circulation over North America could motivate the use of SOK sea ice anomalies for North American seasonal to subseasonal weather prediction. However, the small magnitude of the  $Z_{500}$  anomalies and the lack of significant  $\theta_{850}$  anomalies over North America suggests that the use of interannual SOK sea ice variability for such predictions may be limited. This result does not preclude the potential for more extensive sea ice loss in this region to have notable impacts on atmospheric circulation over North America in the future.

The results from this study raise further questions to be explored. For instance, the composite analysis shows the *average* progression of conditions preceding and following anomalous sea ice coverage, not the progression of conditions that occur in any individual years. The relative importance of interseasonal SST anomalies, autumn thermodynamic preconditioning, and winter mechanical forcing in setting up anomalously low sea ice coverage in the SOK remains an open question. Furthermore, it is not clear from this analysis if each of these mechanisms is present in all anomalous sea ice years or if individual years are affected by a smaller number of mechanisms.

Prediction of maximum sea ice extent in the SOK has already been undertaken with upwards of 70% of total variance explained (Sasaki et al. 2007; Nakanowatari et al. 2010). These predictive models incorporate variables such as 850 mb temperature, offshore components of the geostrophic wind, and SST in the vicinity of the SOK at lead times of one to three months. This study furthers our understanding of the processes responsible for generating interannual variability in sea ice coverage in the SOK, which could help to improve such predictive models. Extending these ideas to examine similar processes within the central Arctic could provide further understanding and predictability of interannual variability in Arctic sea ice coverage as that region eventually becomes seasonally ice-free.

**Acknowledgements** The authors want to thank Sukyoung Lee for helpful insights. Thanks to the Community Earth System Model (CESM) Large Ensemble Community Project for access to CESM model output and to NSF, CISL, and Yellowstone for providing the supercomputing resources necessary for accessing that output. The authors are thankful for access to ERA-Interim reanalysis products for use in this study (European Centre for Medium-range Weather Forecast (ECMWF) (2011): The ERA-Interim reanalysis dataset, Copernicus Climate Change Service (C3S) (first accessed 7-6-2018), available from <https://www.ecmwf.int/en/forecasts/datasets/archive-datasets/reanalysis-datasets/era-interim>). COBE SST data was provided by the NOAA/OAR/ESRL PSD, Boulder, Colorado, USA, from their Web site at <https://www.esrl.noaa.gov/psd/>.

## References

- Alexander MA, Bhatt U, Walsh JE, Timlin MS, Miller JS, Scott JD (2004) The atmospheric response to realistic Arctic sea ice anomalies in an AOGCM during winter. *J Clim* 17:890–905
- Bitz CM, Lipscomb WH (1999) An energy-conserving thermodynamic model of sea ice. *J Geophys Res Oceans* 104(C7):15669–15677. <https://doi.org/10.1029/1999jc900100>
- Blackport R, Screen JA, van der Wiel K, Bintanja R (2019) Minimal influence of reduced Arctic sea ice on coincident cold winters in mid-latitudes. *Nat Clim Change* 9(9):697–704. <https://doi.org/10.1038/s41558-019-0551-4>
- Close S, Houssais MN, Herbaut C (2017) The Arctic winter sea ice quadrupole revisited. *J Clim* 30(9):3157–3167. <https://doi.org/10.1175/JCLI-D-16-0506.1>
- Dee DP, Uppala SM, Simmons AJ, Berrisford P, Poli P, Kobayashi S, Andrae U, Balmaseda MA, Balsamo G, Bauer P, Bechtold P, Beljaars AC, van de Berg L, Bidlot J, Bormann N, Delsol C, Dragani R, Fuentes M, Geer AJ, Haimberger L, Healy SB, Hersbach H, Hólm EV, Isaksen L, Källberg P, Köhler M, Matricardi M, McNally AP, Monge-Sanz BM, Morcrette JJ, Park BK, Peubey C, de Rosnay P, Tavolato C, Thépaut JN, Vitart F (2011) The ERA-Interim reanalysis: configuration and performance of the data assimilation system. *Q J R Meteorol Soc* 137(656):553–597. <https://doi.org/10.1002/qj.828>
- Deser C, Walsh JE, Timlin MS (2000) Arctic sea ice variability in the context of recent atmospheric circulation trends. *J Clim* 13:617–633. [https://doi.org/10.1175/1520-0442\(2000\)013<0617:ASIVI>2.0.CO;2](https://doi.org/10.1175/1520-0442(2000)013<0617:ASIVI>2.0.CO;2)
- Deser C, Alexander MA, Timlin MS (2003) Understanding the persistence of sea surface temperature anomalies in mid-latitudes. *J Clim* 16(1):57–72. [https://doi.org/10.1175/1520-0442\(2003\)016<0057:UTPOSS>2.0.CO;2](https://doi.org/10.1175/1520-0442(2003)016<0057:UTPOSS>2.0.CO;2)
- England M, Jahn A, Polvani L (2019) Nonuniform contribution of internal variability to recent Arctic sea ice loss. *J Clim* 32(13):4039–4053. <https://doi.org/10.1175/JCLI-D-18-0864.1>
- Fang Z, Wallace JM (1994) Arctic sea ice variability on a timescale of weeks and its relation to atmospheric forcing. *J Clim* 7:1897–1914
- Gascard JC, Riemann-Campe K, Gerdes R, Schyberg H, Randriamampianina R, Karcher M, Zhang J, Rafizadeh M (2017) Future sea ice conditions and weather forecasts in the Arctic: implications for Arctic shipping. *Ambio* 46:355–367. <https://doi.org/10.1007/s13280-017-0951-5>
- Gervais M, Atallah E, Gyakum JR, Tremblay LB (2016) Arctic air masses in a warming world. *J Clim* 29:2359–2373. <https://doi.org/10.1175/JCLI-D-15-0499.1>
- Gu Q, Gervais M (2020) Exploring North Atlantic and North Pacific Decadal climate prediction using self-organizing maps. *J Clim* 34(1):123–141. <https://doi.org/10.1175/JCLI-D-20-0017.1>
- Honda MK, Yamazaki K, Takeuchi K (1999) Dynamic and thermodynamic characteristics of atmospheric response to anomalous sea ice extent in the Sea of Okhotsk. *J Climate* 12:3347–3358. [https://doi.org/10.1175/1520-0442\(1999\)012<3347:DATCOA>2.0.CO;2](https://doi.org/10.1175/1520-0442(1999)012<3347:DATCOA>2.0.CO;2)
- Hunke EC, Dukowicz JK (2002) The elastic-viscous-plastic sea ice dynamics model in general orthogonal curvilinear coordinates on a sphere - incorporation of metric terms. *Mon Weather Rev* 130(7):1848–1865. [https://doi.org/10.1175/1520-0493\(2002\)130<1848:tevpsi>2.0.co;2](https://doi.org/10.1175/1520-0493(2002)130<1848:tevpsi>2.0.co;2)
- Hunke EC, Lipscomb WH (2008) CICE: The Los Alamos Sea Ice Model, Documentation, and Software, Version 4.0. Technical Report, Los Alamos National Laboratory Technical Report LACC-06-012
- Hurrell JW, Neale RB, Large WG, Marsh DR, Lawrence D, Hack JJ, Vavrus S, Ghan S, Lamarque JF, Kushner PJ, Rasch P, Collins WD, Kay JE, Vertenstein M, Kiehl J, Holland MM, Lipscomb WH, Long MC, Lindsay K, Gent PR, Marshall S, Bader D, Mahowald N (2013) The community earth system model: a framework for collaborative research. *Bull Am Meteorol Soc* 94(9):1339–1360. <https://doi.org/10.1175/bams-d-12-00121.1>
- Ishii M, Shouji A, Sugimoto S, Matsumoto T (2005) Objective analyses of sea-surface temperature and marine meteorological variables for the 20th century using ICOADS and the Kobe Collection. *Int J Climatol* 25(7):865–879. <https://doi.org/10.1002/joc.1169>
- Jahn A, Kay JE, Holland MM, Hall DM (2016) How predictable is the timing of a summer ice-free Arctic? *Geophys Res Lett* 43:9113–9120. <https://doi.org/10.1002/2016GL070067>
- Kay JE, Deser C, Phillips A, Mai A, Hannay C, Strand G, Arblaster JM, Bates SC, Danabasoglu G, Edwards J, Holland M, Kushner P, Lamarque JF, Lawrence D, Lindsay K, Middleton A, Munoz E, Neale R, Oleson K, Polvani L, Vertenstein M (2015) The community earth system model (CESM) large ensemble project: a

- community resource for studying climate change in the presence of internal climate variability. *Bull Am Meteorol Soc* 96(8):1333–1349. <https://doi.org/10.1175/BAMS-D-13-00255.1>
- Kimura N, Wakatsuchi M (1999) Processes controlling the advance and retreat of sea ice in the Sea of Okhotsk. *J Geophys Res* 104(C5):11137–11150
- Lawrence DM, Oleson KW, Flanner MG, Thornton PE, Swenson SC, Lawrence PJ, Zeng X, Yang ZL, Levis S, Sakaguchi K, Bonan GB, Slater AG (2011) Parameterization improvements and functional and structural advances in Version 4 of the Community Land Model. *J Adv Mod Earth Syst* 3(1):1–27. <https://doi.org/10.1029/2011ms00045>
- Meier W, Fetterer F, Savoie M, Mallory S, Duerr R, Stroeve J (2017) NOAA/NSIDC Climate Data Record of Passive Microwave Sea Ice Concentration, Version 3. [Dataset] [Feb. 1980–Feb. 2000]. <https://doi.org/10.7265/N59P2ZTG>, [6 Jul 2018]
- Melia N, Haines K, Hawkins E, Day JJ (2017) Towards seasonal Arctic shipping route predictions. *Environ Res Lett*. <https://doi.org/10.1088/1748-9326/aa7a60>
- Mesquita MD, Hodges KI, Atkinson DE, Bader J (2011) Sea-ice anomalies in the Sea of Okhotsk and the relationship with storm tracks in the Northern Hemisphere during winter. *Dyn Meteorol Oceanogr Tellus Ser A*. <https://doi.org/10.1111/j.1600-0870.2010.00483.x>
- Nakanowatari T, Ohshima KI, Nagai S (2010) What determines the maximum sea ice extent in the Sea of Okhotsk? Importance of ocean thermal condition from the Pacific. *J Geophys Res Oceans* 115(12):1–10. <https://doi.org/10.1029/2009JC006070>
- Ogi M, Tachibana Y (2006) Influence of the annual Arctic Oscillation on the negative correlation between Okhotsk Sea ice and Amur River discharge. *Geophys Res Lett* 33(8):2–5. <https://doi.org/10.1029/2006GL025838>
- Ogi M, Taguchi B, Honda M, Barber DG, Rysgaard S (2015) Summer-to-winter sea-ice linkage between the Arctic ocean and the Okhotsk sea through atmospheric circulation. *J Clim* 28(12):4971–4979. <https://doi.org/10.1175/JCLI-D-14-00297.1>
- Ohshima KI, Nihashi S, Hashiya E, Watanabe T (2006) Interannual Variability of Sea Ice Area in the Sea of Okhotsk: Importance of Surface Heat Flux in Fall. *J Meteorol Soc Jpn* 84(5):907–919
- Oleson KW, Lawrence DM, Bonan GB, Flanner MG, Kluzek E, Lawrence PJ, Levis S, Swenson SC, Thornton PE (2010) Technical description of version 4.0 of the Community Land Model (CLM)
- Peng G, Meier WN, Scott DJ, Savoie MH (2013) A long-term and reproducible passive microwave sea ice concentration data record for climate studies and monitoring. *Earth Syst Sci Data*. <https://doi.org/10.5194/essd-5-311-2013>
- Rosenblum E, Eisenman I (2017) Sea ice trends in climate models only accurate in runs with biased global warming. *J Clim* 30(16):6265–6278. <https://doi.org/10.1175/JCLI-D-16-0455.1>
- Rothrock DA (1975) The energetics of the plastic deformation of pack ice by ridging. *J Geophys Res* 80(33):4514–4519
- Sasaki YN, Katagiri Y, Minobe S, Rigor IG (2007) Autumn atmospheric preconditioning for interannual variability of wintertime sea-ice in the Okhotsk Sea. *J Oceanogr* 63(2):255–265. <https://doi.org/10.1007/s10872-007-0026-5>
- Screen JA (2017) Simulated atmospheric response to regional and pan-arctic sea ice loss. *J Clim* 30(11):3945–3962. <https://doi.org/10.1175/JCLI-D-16-0197.1>
- Smith R, Jones P, Briegleb B, Bryan F, Danabasoglu G, Dennis J, Dukowicz JK, Eden C, Fox-Kemper B, Gent P, Hecht M, Jayne S, Jochum M, Large W, Lindsay K, Maltrud M, Norton N, Peacock S, Vertenstein M, Yeager S (2010) The Parallel Ocean Program (POP) reference manual: Ocean component of the Community Climate System Model (CCSM) and Community Earth System Model (CESM). Technical report, Los Alamos National Laboratory Technical report LAUR-10-01853, <http://www.cesm.ucar.edu/models/cesm1.0/pop2/doc/sci/POPRefManual.pdf>
- Sun L, Deser C, Tomas RA (2015) Mechanisms of stratospheric and tropospheric circulation response to projected Arctic sea ice loss. *J Clim* 28(19):7824–7845. <https://doi.org/10.1175/JCLI-D-15-0169.1>
- Takaya K, Nakamura H (2001) A formulation of a phase-independent wave-activity flux for stationary and migratory quasigeostrophic eddies on a zonally varying basic flow. *J Atmos Sci* 58(6):608–627. [https://doi.org/10.1175/1520-0469\(2001\)058<0608:AFOAP>2.0.CO;2](https://doi.org/10.1175/1520-0469(2001)058<0608:AFOAP>2.0.CO;2)
- Thompson DWJ, Wallace JM (1998) The Arctic oscillation signature in the wintertime geopotential height and temperature fields. *Geophys Res Lett* 25(9):1297. <https://doi.org/10.1029/98GL00950>
- Thorndike AS, Rothrock DA, Maykut GA, Colony R (1975) The thickness distribution of sea ice. *J Geophys Res* 80(33):4501–4513. <https://doi.org/10.1029/jc080i033p04501>
- Ukita J, Honda M, Nakamura H, Tachibana Y, Cavalieri DJ, Parkinson CL, Koide H, Yamamoto K (2007) Northern Hemisphere sea ice variability: lag structure and its implications. *Tellus Ser A Dyn Meteorol Oceanogr* 59(2):261–272. <https://doi.org/10.1111/j.1600-0870.2006.00223.x>
- Yamamoto K, Tachibana Y, Honda M, Ukita J (2006) Intra-seasonal relationship between the Northern Hemisphere sea ice variability and the North Atlantic Oscillation. *Geophys Res Lett* 33(14):2–6. <https://doi.org/10.1029/2006GL026286>
- Yeager SG, Danabasoglu G, Rosenbloom NA, Strand W, Bates SC, Meehl GA, Karspeck AR, Lindsay K, Long MC, Teng H, Loveniuski NS (2018) Predicting near-term changes in the earth system: a large ensemble of initialized decadal prediction simulations using the community earth system model. *Bull Am Meteorol Soc* 99(9):1867–1886. <https://doi.org/10.1175/BAMS-D-17-0098.1>

**Publisher's Note** Springer Nature remains neutral with regard to jurisdictional claims in published maps and institutional affiliations.